Weak and strong from meshless methods for linear elastic problem under fretting contact conditions

Gregor Kosec[a], Jure Slak[a,b], Matjaž Depolli[a], Roman Trobec[a], Kyvia Pereira[c], Satyendra Tomar[d], Thibault Jacquemin[d], Stéphane P.A. Bordas[e,d], Magd Abdel Wahab[f,g,h]

[a] *Parallel and Distributed Systems Laboratory, "Jožef Stefan" Institute, Jamova 39, Ljubljana, Slovenia*
[b] *Faculty of Mathematics and Physics, University of Ljubljana, Jadranska 19, Ljubljana, Slovenia*
[c] *Department of Electrical Energy, Systems and Automation, Faculty of Engineering and Architecture, Ghent University, Belgium*
[d] *Institute of Computational Engineering, University of Luxembourg, 6 Avenue de la Fonte, 4364 Esch-sur-Alzette, Luxembourg*
[e] *Visiting Professor, Institute of Research and Development, Duy Tan University, K7/25 Quang Trung, Danang, Vietnam*
[f] *Division of Computational Mechanics, Ton Duc Thang University, Ho Chi Minh City, Vietnam*
[g] *Faculty of Civil Engineering, Ton Duc Thang University, Ho Chi Minh City, Vietnam*
[h] *Soete Laboratory, Faculty of Engineering and Architecture, Ghent University, Technologiepark Zwijnaarde 903, Zwijnaarde B, 9052, Belgium*

Abstract

We present numerical computation of stresses under fretting fatigue conditions derived from closed form expressions. The Navier-Cauchy equations, that govern the problem, are solved with strong and weak form meshless numerical methods. The results are compared to the solution obtained from well-established commercial package ABAQUS, which is based on finite element method (FEM). The results show that the weak form meshless solution exhibits similar behaviour as the FEM solution, while, in this particular case, strong form meshless solution performs better in capturing the peak in the surface stress. This is of particular interest in fretting fatigue, since it directly influences crack initiation. The results are presented in terms of von Mises stress contour plots, surface stress profiles, and the convergence plots for all three methods involved in the study.

Keywords: MLSM, MLPG, Navier equation, convergence, meshless, meshfree, fracture, crack, fretting fatigue

1. Introduction

Two loaded surfaces in contact, that are exposed to a relative oscillatory movement, experience fretting fatigue. Fretting fatigue tangibly downgrades the surface layer quality, producing increased surface roughness and micropits, which reduces the fatigue strength of the components up to 50% [1]. The phenomenon is present in many mechanical assemblies, e.g. bolted joints, shrink-fitted shafts, etc., and it is, therefore, a critical research topic [2]. Even though crystal plasticity, metallurgical changes, and thermomechanical effects may significantly impact fretting fatigue [3], their effects have been ignored in many recent numerical life predictions of fretting [4, 5, 6]. Generally, the problem is simplified, and the numerical models rely on the computation of stress fields near the contact region, obtained either by analytical solutions or by finite element analysis. Those stress fields, in conjunction with fracture mechanics approaches, are used to predict crack initiation and propagation lives under partial slip conditions with reasonable accuracy [7, 8]. In this regard, the efficient estimation of the stress field around the contact area is still of great importance.

The complexity of the fretting fatigue phenomenon arises from the presence of the sticking and sliding regimes at the contact interface, which play an important role on the crack initiation zone. A common way to identify these regimes is to observe the contact surface of samples after test [9, 7], the undamaged and unworn part is considered to be sticking while the slip region is characterized by worn out and damaged area.

Therefore, a surface discontinuity is created at the stick-slip boundary. Characterization of stick-slip zones may also be achieved by analysing curves of tangential loads Q with respect to the applied normal load P (Q-P curves) In [10, 11] authors proposed fretting maps that considered the influence of normal load, sliding displacement and wear on the stick-slip regime. Regarding simulation methods, many researches consider numerical stress analysis of contact to study the stick-slip zone, for example, in [12, 13, 6].

Recent laboratory studies [14] indicated that the stress field could experience singularity at the transition between sticking and sliding regimes. However, in a recent numerical investigation of fretting fatigue, the authors demonstrated the absence of singularities in the stress field [15]. This paper extends the discussion from [15] by comparing three conceptually different numerical approaches for the solution of a stress field in the contact area, with the ultimate goal to establish confidence in the numerical solution of the stress field in a typical fretting fatigue simulation. In this paper the contact is mimicked by surface normal and tangential traction loads derived from closed form expressions [2]. More details on treatment of the contact in meshless context can be found in [16, 17, 18].

From the numerical point of view, the most difficult part of fretting fatigue simulations is the computation of the stress tensor within the bodies in play, by solving the Navier-Cauchy partial differential equations (PDEs). When comparing two classes of numerical methods, namely, the weak form methods and the strong form methods, the conceptual difference between them is that strong form methods solve the underlying problem in its strong, differential form, directly approximating partial differential operators appearing in the equation. On the other hand, weak form methods solve the weak formulation of the problem, which reduces derivative order by using integral theorems. The discretization of the equation is done by weakly imposing the equation in each element or subdomain, and by choosing appropriate subspaces where the solution is sought.

Traditionally, the Navier-Cauchy equations are tackled in their weak form with the Finite Element Method (FEM) [19]. However, linear elasticity problems have also been investigated with alternative meshless methods [20], in both forms, strong and weak [21, 22, 23], and with different conclusions. For example, the strong form solution based on a generalised diffuse derivative approximation, combined with a point collocation, is reported to provide excellent results [24]. Also, in a recent paper [21], the authors use a strong form method, based on augmented collocation with radial basis functions, and report good behavior. The literature also reports that meshless collocation approaches are not well-suited for contact and fretting problems. Hermite type collocation was proposed as a remedy, but this was shown to lead to lower accuracy compared to the FEM solution [25].

The conceptual difference between meshless methods and mesh-based methods is in the treatment of relations between nodes. In mesh-based methods the nodes need to be structured into polygons (mesh) that covers the whole computational domain, while on the other hand, meshless methods define relations between nodes directly through the relative nodal positions [26]. An immediate consequence of such a simplification is greater generality regarding the approximation, and the position of computational points, both crucial for dealing with large gradients or possibly singular behavior, e.g. at the corner between a pad contacting with a specimen, or at a crack tip. This flexibility in point placement comes at the price of the need to identify neighboring nodes, and, for weak form based methods, leads to computationally expensive integration of usually non-polynomial functions [20], which also occurs in methods such as isogeometric analysis [27].

The most well-known mesh-based strong form method is the Finite Difference Method (FDM) that was later generalized into many meshless variants in pursuit of greater freedom regarding the selection of approximation type and lesser geometric limitations, see [28, 29, 30] for some early references.

In meshless methods, instead of predetermined interpolation over a local support, a more general approach with variable support and basis functions is used, e.g. collocation using Radial Basis Functions [31] or approximation with monomial basis [32]. There are many other methods with more or less similar methodology introducing new variants of the strong form meshless principle [20].

Meshless methods are not restricted by the choice of material behaviour, and are fully general. However, point collocation methods are not naturally suited to tackling plasticity, mainly because the discretised gradient operator used to compete the left hand side (stiffness matrix) has to be strictly identical to that used to compute the right hand side (residual vector), to ensure convergence of Newton Raphson. This is

however possible, as was shown in the literature [33, 34, 35].

In spite of decades of research on meshfree and meshless methods, starting with the work of Monaghan on smoothed particle hydrodynamics [36], and later complemented by the inception of Galerkin meshfree methods such as the Element-Free Galerkin method (EFG) [37], there is no consensus today on the relative performance of various meshfree methods, which is clearly problem dependent. For example, enriched meshfree methods have emerged to cope with the inability of original formulations to deal with discontinuities, strong or weak, as well as singularities and boundary layers.

Spurred by the advent of massively parallel computing on chips, such as graphical processing units (GPUs) and similar multi-threaded architectures, either used in isolation or in concert with CPUs, a recent trend has been to develop meshless collocation approaches for PDEs, because they allow the assembly of nodal equations completely independently. Two classes of collocation schemes have surfaced: (1) those relying on field approximation, such as the isogeometric collocation approach [38], or: (2) on directly approximating the discretization operator [39]. The mathematics community has put significant effort in understanding the approximation properties of both classes of methods [40].

On the other hand, weak form meshless methods are generalizations of mesh-based weak form FEM. An overarching framework, which can be seen as a superset of most meshfree methods, is the Meshless Local Petrov Galerkin Method (MLPG) [41]. There exist different variants of MLPG, which include Bubnov-Galerkin, Petrov-Galerkin and collocation methods. The different variants are obtained through the choice of the trial and test spaces [20]. In the weak-form based approaches, test and trial functions may be chosen as Moving Least Squares approximants. Contrary to FEM, where the main loop is generally over the elements, in MLPG and most weak-form based meshless methods, the main loop is performed over the integration points. For each integration point, a local support is used to evaluate field values and weight functions. In the last few decades, there have been many variants of MLPG introduced to mitigate numerical instabilities and to improve accuracy and convergence rate, etc. [20]. In this paper, we will use a more general formulation of Meshless Local Strong Form Method (MLSM) [26].

The rest of the paper is organized as follows: in Section 2, the governing problem is introduced, Section 3 is focused on meshless numerical techniques, and Section 4 focuses on presentation and discussion of results.

2. Governing problem

Displacements and stresses are quantities of interest in analyses of solid bodies under loading conditions. The stresses are expressed with the stress tensor $\boldsymbol{\sigma}$ and are related to displacements $\vec{u}$ via Hooke's law:

$$\boldsymbol{\sigma} = \boldsymbol{C} : \boldsymbol{\varepsilon}, \quad \boldsymbol{\varepsilon} = \frac{1}{2}(\nabla\vec{u} + (\nabla\vec{u})^{\mathsf{T}}), \tag{1}$$

where C is the fourth order stiffness tensor. The traction to any surface with normal $\vec{n}$ is given as $\vec{t} = \boldsymbol{\sigma}\vec{n}$. Only isotropic homogeneous materials will be considered in this paper, which simplifies C to

$$C_{ijkl} = \tilde{\lambda}\delta_{ij}\delta_{kl} + \tilde{\mu}(\delta_{ik}\delta_{jl} + \delta_{il}\delta_{jk}), \tag{2}$$

where $\tilde{\lambda}$ and $\tilde{\mu}$ are material's Lamé parameters. Note that the letter μ is later used for the coefficient of friction. The equilibrium equation for forces and moments is a form of a Cauchy momentum equation:

$$\nabla \cdot \boldsymbol{\sigma} = \vec{f}, \tag{3}$$

where $\vec{f}$ is the body force. For strong form methods, the Cauchy-Navier equation is used, obtained by substituting (1) into (3):

$$(\tilde{\lambda} + \tilde{\mu})\nabla(\nabla \cdot \vec{u}) + \tilde{\mu}\nabla^2\vec{u} = 0. \tag{4}$$

For weak form methods, the Cauchy momentum equation (3) is reformulated to its weak form counterpart. The solution $\vec{u}$ satisfies

$$\int_\Omega \boldsymbol{\sigma}(\vec{u}) : \boldsymbol{\varepsilon}(\vec{v})\, dV - \int_{\partial\Omega} \vec{t}(\vec{u}) \cdot \vec{v}\, dS - \int_\Omega \vec{f} \cdot \vec{v}\, dV = 0, \tag{5}$$

for every test function $\vec{v}$ from a suitable function space, where Ω represents the domain and $\partial\Omega$ its boundary.

Two types of boundary conditions are usually specified, referred to as essential or Dirichlet boundary conditions, and traction or natural boundary conditions. Essential boundary conditions specify displacements on some portion of the boundary of the domain, i.e. $\vec{u} = \vec{u}_0$, while traction boundary conditions specify surface traction $\boldsymbol{\sigma}\vec{n} = \vec{t}_0$, where $\vec{n}$ is an outside unit normal to the boundary of the domain.

In two dimensions, we will use simplified component-wise notation for $\vec{u}$ and $\boldsymbol{\sigma}$:

$$\vec{u} = (u, v) \quad \text{and} \quad \boldsymbol{\sigma} = \begin{bmatrix} \sigma_{xx} & \sigma_{xy} \\ \sigma_{xy} & \sigma_{yy} \end{bmatrix}. \tag{6}$$

2.1. Case definition

The case analyzed in this paper is the same as the one discussed in Pereira et al. [15]. A small thin rectangular specimen of width W, length L and thickness t made of aluminum AA2420-T3 is considered. The specimen is stretched in one axis with oscillatory axial traction $\boldsymbol{\sigma}_{ax}$, normally compressed in another axis by two cylindrical pads with force F, that additionally act tangent to the surface with force Q, and thus producing tangential traction. The setup is shown schematically in Figure 1a.

The analytical model for surface tractions is employed to obtain suitable boundary conditions for numerical simulations. Contact tractions are modeled using an extension of Hertzian contact theory [2], predicting the contact half-width

$$a = 2\sqrt{\frac{FR}{t\pi E^*}}, \tag{7}$$

where E^* is the combined Young's modulus, computed as $\frac{1}{E^*} = \frac{1-\nu_1^2}{E_1} + \frac{1-\nu_2^2}{E_2}$, where E_i and ν_i represent the Young's moduli and Poisson's ratios of the specimen and the pad, respectively.

Normal traction p is computed as in Hertzian contact theory

$$p(x) = \begin{cases} p_0\sqrt{1-\frac{x^2}{a^2}}, & |x| \leq a \\ 0, & |x| > a \end{cases}, \quad p_0 = \sqrt{\frac{FE^*}{t\pi R}}, \tag{8}$$

where $\frac{F}{t}$ represents the force per unit thickness, and p_0 is the maximal pressure.

Due to the presence of tangential traction, the effect of friction is modeled by splitting the surface under contact into two zones, stick and slip zones. The parameters c and e, representing stick zone half-width and eccentricity due to axial loading, respectively, are computed as

$$c = a\sqrt{1-\frac{Q}{\mu f}}, \quad e = \operatorname{sgn}(Q)\frac{a\boldsymbol{\sigma}_{ax}}{4\mu p_0}, \tag{9}$$

where μ is the coefficient of friction.

Tangential traction $q(x)$, dependent on the coefficient of friction μ, is defined as

$$q(x) = \begin{cases} -\mu p(x) + \frac{\mu p_0 c}{a}\sqrt{1-\frac{(x-e)^2}{c^2}}, & |x-e| < c, \\ -\mu p(x), & c \leq |x-e|, |x| \leq a, \\ 0, & |x| > a. \end{cases} \tag{10}$$

Additionally, the tangential force Q must be smaller than the maximal permitted force μF, predicted by Coulomb's law, to be possible to define the stick half-width c. There is also an upper bound for axial traction $\boldsymbol{\sigma}_{ax}$ given by (10), implying the limit $\boldsymbol{\sigma}_{ax} \leq 4(1-\frac{c}{a})$. Both of these inequalities are satisfied in all our examples.

We assume that plane strain conditions are valid, and thus, reduce the problem to two dimensions, and use symmetry along the horizontal axis. The domain Ω for numerical simulations, which represents half the specimen, is given by

$$\Omega = [-L/2, L/2] \times [-W/2, 0]. \tag{11}$$

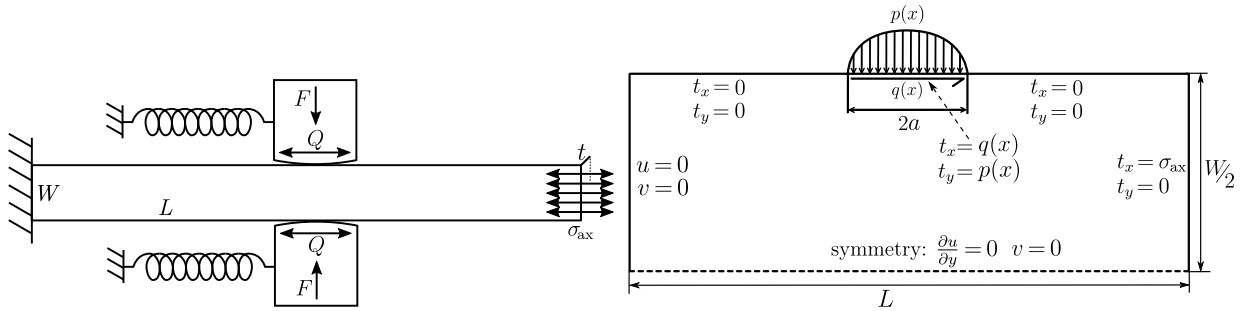

(a) Scheme of the experiment.

(b) Numerical domain and boundary conditions.

Figure 1: Case description. Ratios in drawings are not to scale.

The boundary conditions, that are used for numerical simulations, are illustrated in Figure 1b. Note that symmetry boundary conditions are used on the bottom boundary. All parameters are set as in [15]:

Specimen dimensions: $L = 40\,\text{mm}$, $W = 10\,\text{mm}$ and $t = 4\,\text{mm}$,

Material parameters: $E_1 = E_2 = 72.1\,\text{GPa}$, $\nu_1 = \nu_2 = 0.33$,

Forces and tractions: $F = 543\,\text{N}$, $Q = 155\,\text{N}$, $\boldsymbol{\sigma}_{ax} = 100\,\text{MPa}$.

The effect of cylinder pads is completely characterized by their pad radii. Two different pad radii, $R = 10\,\text{mm}$ and $R = 50\,\text{mm}$ were considered, each for two different coefficients of friction, $\mu = 0.3$ and $\mu = 2$, resulting in four numerical examples with derived parameters specified in Table 1.

	$\mu = 0.3$	$\mu = 2$
$R = 10\,\text{mm}$	$a = 0.2067\,\text{mm}$	$a = 0.2067\,\text{mm}$
	$p_0 = 418.1041\,\text{MPa}$	$p_0 = 418.1041\,\text{MPa}$
	$c = 0.0450\,\text{mm}$	$c = 0.1914\,\text{mm}$
	$e = 0.0412\,\text{mm}$	$e = 0.0062\,\text{mm}$
$R = 50\,\text{mm}$	$a = 0.4622\,\text{mm}$	$a = 0.4622\,\text{mm}$
	$p_0 = 186.9818\,\text{MPa}$	$p_0 = 186.9818\,\text{MPa}$
	$c = 0.1007\,\text{mm}$	$c = 0.4279\,\text{mm}$
	$e = 0.2060\,\text{mm}$	$e = 0.0309\,\text{mm}$

Table 1: Derived parameter values for all four considered cases.

The top boundary conditions, given by tractions $p(x)$ and $q(x)$, are illustrated for all four cases in Figure 2. As seen also from Table 1, the pad with larger radius has lower normal traction than its smaller counterpart. A coefficient of friction μ has a clear effect on the stress profile, as it causes significant stress concentrations and high gradients near the edges of stick and slip zones.

3. Meshless numerical method

The main goal of this paper is to compare different numerical methods for solution of linear elasticity problem under contact conditions, which are not considered in this paper. Instead, a simplified model with boundary conditions that mimic frictional contact through normal and tangential traction loads derived from closed form expressions [2] is used.

In this section, two conceptually different meshless methods are described. We first describe the Meshless Local Strong Form method (MLSM) [22], a meshless method solving problems in strong form, which is

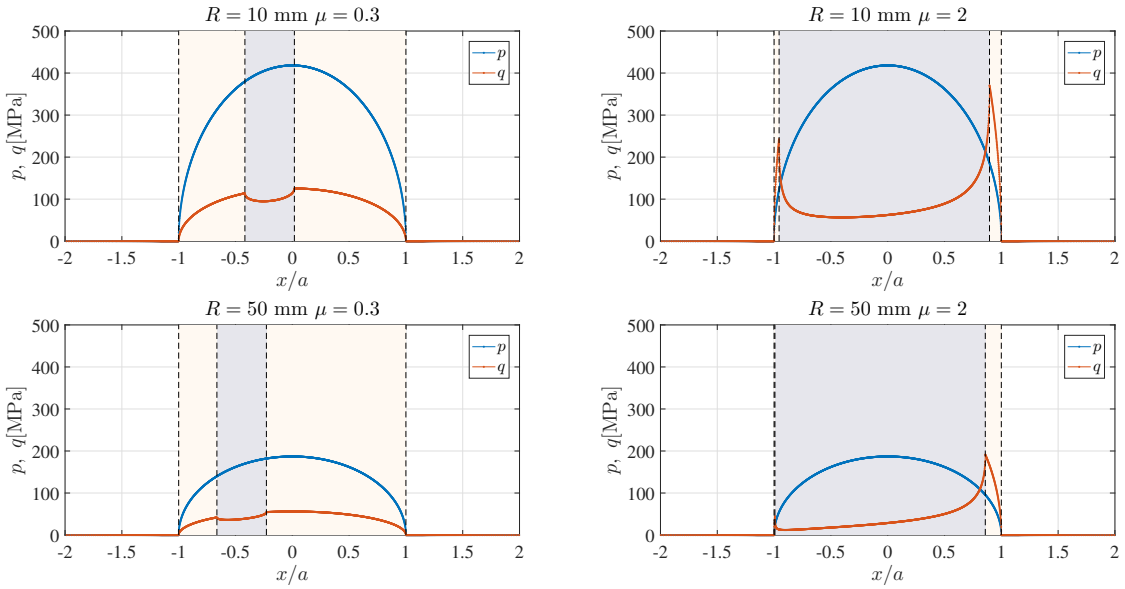

Figure 2: Top traction profiles p and q for four considered cases. The stick zone is shown in the gray color, and the slip zone is shown in the beige color.

followed by the Meshless Local Petrov Galerkin (MLPG) method [42], a weak form meshless numerical method. The common methodology of both methods is the Moving Least Squares (MLS) approximation, which is described first.

3.1. MLS approximation

A generalized MLS approximant $\hat{u}$, introduced by Shepard [43], and later generalized from monomials to1 arbitrary basis functions such as Radial Basis Functions (RBFs), is defined by

$$\hat{u}(\boldsymbol{x}) = \sum_{j=1}^{m} \alpha_j(\boldsymbol{x}) b_j(\boldsymbol{x}) \equiv \boldsymbol{b}^{\mathsf{T}}(\boldsymbol{x})\boldsymbol{\alpha}(\boldsymbol{x}), \tag{12}$$

where b_j are basis functions. For example, a quadratic monomial basis in a two-dimensional domain is provided by

$$\boldsymbol{b}^{\mathsf{T}}(x, y) = [1, x, y, x^2, y^2, xy], \quad m = 6. \tag{13}$$

The unknown coefficients $\alpha_j(\boldsymbol{x})$ in Equation (12) are not constant, but also functions of $\boldsymbol{x}$ (hence the name "moving"). At any point $\boldsymbol{x}$ with n neighboring nodes, that constitute its support domain, coefficients $\alpha_j(\boldsymbol{x})$ can be obtained by minimizing

$$R^2 = \sum_{i=1}^{n} w(\boldsymbol{x} - \boldsymbol{x}_i)(u(\boldsymbol{x}_i) - \boldsymbol{b}^{\mathsf{T}}(\boldsymbol{x}_i)\boldsymbol{\alpha}(\boldsymbol{x}))^2, \tag{14}$$

where $w\colon \mathbb{R} \to \mathbb{R}$ is a non-negative weight function, and $\boldsymbol{x}_i$ are the neighboring points. Minimizing (14) with respect to $\boldsymbol{x}$ yields a system of equations of the form

$$A(\boldsymbol{x})\boldsymbol{\alpha}(\boldsymbol{x}) = B(\boldsymbol{x})\boldsymbol{u}, \tag{15}$$

where $\boldsymbol{\alpha}(\boldsymbol{x})$ are the unknown coefficients, $\boldsymbol{u}$ are the function values in support nodes, $A(\boldsymbol{x}) = \sum_{i=1}^{n} w(\boldsymbol{x} - \boldsymbol{x}_i)\boldsymbol{b}(\boldsymbol{x})\boldsymbol{b}(\boldsymbol{x})^{\mathsf{T}}$, and $B(\boldsymbol{x}) = [\boldsymbol{w}(\boldsymbol{x} - \boldsymbol{x}_1)\boldsymbol{b}(x_1), \ldots, \boldsymbol{w}(\boldsymbol{x} - \boldsymbol{x}_n)\boldsymbol{b}(x_n)]$. Solving (15) for $\boldsymbol{\alpha}(\boldsymbol{x})$, and substituting it into (12) we obtain

$$\hat{u}(\boldsymbol{x}) = \boldsymbol{b}(\boldsymbol{x})^{\mathsf{T}}[A(\boldsymbol{x})]^{-1}B(\boldsymbol{x})\boldsymbol{u} = \boldsymbol{\varphi}^{\mathsf{T}}(\boldsymbol{x})\boldsymbol{u}. \tag{16}$$

From (16), we can immediately write the MLS shape functions as

$$\boldsymbol{\varphi}^{\mathsf{T}}(\boldsymbol{x}) = \boldsymbol{b}(\boldsymbol{x})^{\mathsf{T}}[A(\boldsymbol{x})]^{-1}B(\boldsymbol{x}). \tag{17}$$

One can also compute the derivatives of $\hat{u}$ simply by differentiating the shape functions. For example, the first derivative is given by

$$\begin{aligned}\frac{\partial \boldsymbol{\varphi}}{\partial x_k}(\boldsymbol{x}) = &\frac{\partial \boldsymbol{b}^{\mathsf{T}}}{\partial x_k}(\boldsymbol{x})[A(\boldsymbol{x})]^{-1}B(\boldsymbol{x}) \\ &- \boldsymbol{b}^{\mathsf{T}}(\boldsymbol{x})[A(\boldsymbol{x})]^{-1}\frac{\partial A}{\partial x_k}(\boldsymbol{x})[A(\boldsymbol{x})]^{-1}B(\boldsymbol{x}) + \boldsymbol{b}^{\mathsf{T}}(\boldsymbol{x})[A(\boldsymbol{x})]^{-1}\frac{\partial B}{\partial x_k}(\boldsymbol{x}).\end{aligned} \tag{18}$$

3.2. MLSM formulation

The Meshless Local Strong Form method is a generalization of several strong form meshless methods reported in literature, e.g. the Finite Point Method [44], RBF-FD method [45], Diffuse Approximate Method [32], Local Radial Basis Function Collocation Method [31], etc. A PDE $\mathcal{L}u = f$ is imposed at nodes by means of direct evaluation of differential operators, i.e. operator $\mathcal{L}$ is approximated at a point $\boldsymbol{p}$ as

$$(\mathcal{L}u)(\boldsymbol{p}) \approx (\mathcal{L}\hat{u})(\boldsymbol{p}) = (\mathcal{L}\boldsymbol{\varphi})(\boldsymbol{p})^{\mathsf{T}}\boldsymbol{u}, \tag{19}$$

where $\mathcal{L}\boldsymbol{\varphi}$ is approximated as

$$(\mathcal{L}\boldsymbol{\varphi})(\boldsymbol{p})^{\mathsf{T}} \approx (\mathcal{L}\boldsymbol{b}^{\mathsf{T}})(\boldsymbol{p})A(\boldsymbol{p})^{-1}B(\boldsymbol{p}). \tag{20}$$

In a case when the number of support points is the same as the number of basis functions, this approximation is exact. If the basis $\boldsymbol{b}$ consists of monomials, this method reproduces the Finite Point Method, and if the basis $\boldsymbol{b}$ consists of radial basis functions, centered in support nodes, the operator approximation is the same as in RBF-FD or Local Radial Basis Function Collocation Method.

Using (19), the PDE $\mathcal{L}u = f$ can be approximated at each internal node $\boldsymbol{p}$ with the linear equation

$$(\mathcal{L}\boldsymbol{\varphi})(\boldsymbol{p})^{\mathsf{T}}\boldsymbol{u} = \boldsymbol{f}. \tag{21}$$

For the N_b boundary nodes, the Dirichlet conditions can be imposed directly as long as the approximation scheme is interpolatory, i.e. possesses the Kronecker Delta property [20], while Neumann boundary conditions are discretized in a similar fashion as the equation itself. Gathering all the equations leads to a sparse linear global system with $O(Nn)$ nonzero elements, which can be solved to obtain a numerical approximation of u at N discretization points. For more detailed description of MLSM, the reader is referred to [22].

3.3. MLPG formulation

The MLPG method [42] is based on the weak formulation of a problem

$$\int_\Omega (\mathcal{L}_1 u)(\mathcal{L}_2 v)\, dV - \int_{\partial\Omega} (\vec{n}\cdot\mathcal{L}_3 u)v\, dS - \int_\Omega fv\, dV = 0, \tag{22}$$

where u is the unknown solution and v is a test function. Unlike FEM, which interpolates the trial solution with shape functions, the MLPG approximates it with MLS shape functions (17). The MLS approximant $\hat{u}(\boldsymbol{x})$ is required to satisfy the weak form in the neighborhood of every internal node $\boldsymbol{x}_i = (x_i, y_i)$, by using a suitable test function, which in our case is a compactly supported hat shaped function

$$w_i(x,y) = \max\left\{\left(1 - \left(\frac{x-x_i}{d_i/2}\right)^2\right)\left(1 - \left(\frac{y-y_i}{d_i/2}\right)^2\right),\ 0\right\}, \tag{23}$$

Therefore, integration of (22) only needs to be performed over a local square subdomain Q_i with side d_i,

$$Q_i = \operatorname{supp} w_i = [x_i - d_i/2, x_i + d_i/2] \times [y_i - d_i/2, y_i + d_i/2]. \tag{24}$$

Substituting w_i for v and $\hat{u}$ for u into (22), the following equation is obtained for each internal node x_i:

$$\int_{\Omega_{Q_i}} (\mathcal{L}_1 \hat{u})(\mathcal{L}_2 w_i)\, dV - \int_{\partial\Omega_{Q_i}} (\vec{n} \cdot \mathcal{L}_3 \hat{u}) w_i\, dS - \int_{\Omega_{Q_i}} f w_i\, dV = 0. \tag{25}$$

Note that unless Ω_{Q_i} intersect $\partial\Omega$, the boundary integral over $\partial\Omega_{Q_i}$ vanishes, due to w_i being compactly supported. Substituting the definition of $\hat{u}$ from (16) into (25), a linear equation for unknowns u_i is obtained. The coefficients of this equation are not computed exactly but rather approximated using Gaussian quadrature formulas on n_q points. Note that each computation of the integrand requires the computation of MLS shape function $\boldsymbol{\varphi}$ or its derivatives. Assembling all equations together, a global system of equations is obtained. Essential boundary conditions can not be imposed directly, as MLS shape functions do not possess the Kronecker δ property. Therefore, the value of u is not necessarily reproduced by $\hat{u}$. A common method for imposing boundary conditions is using collocation, i.e. instead of requesting $u = u_0$, a condition $\hat{u} = u_0$ is imposed for every boundary node. Adding this equations to the global system, a sparse $N \times N$ system is obtained, which can be solved using standard procedures to obtain a numerical approximation of u.

Regarding the calibration parameters, calibrating shape parameters for radial basis function is well researched [46], but no special calibration was necessary in our case. The chosen values were default values of the appropriate order of magnitude, such as 1 or 100. The behavior of the methods themselves is well researched and comparisons of the methods on test problems have been performed before [47]. Both methods behave well on the test problems and converge with expected orders of accuracy.

4. Results and discussion

4.1. Comparison of meshless and ABAQUS results

We first present the results of the meshless techniques, and then compare them with the results obtained from a well established commercially available software ABAQUS®. The model consists only of the half specimen part and the effect of pad contact interaction has been replaced by normal and tangential traction loads at contact interface. These loading and boundary conditions are the ones discussed in section 2.1 (summarized in Figure 1b). The symmetric boundary condition is applied to the bottom of the specimen model. One side of the specimen is restricted to move in x and y directions (as in the experiemental set-up), while the maximum cyclic axial load is applied to the other side of the specimen. The analysis considered a purely elastic material, aluminum 2420-T3, with typical material properties, also described in section 2.1. The model has been meshed using with 2D quadrilateral bilinear, plane strain, reduced integration element (CPE4R) and also with 2D quadrilateral quadratic, plane strain, reduced integration element (CPE8R). The model dimensions and also the partitions and seeds used in the ABAQUS analysis are the same as the ones used in [15].

For a complete analysis in ABAQUS considering the contact interaction between pad and specimen (using Lagrange multipliers method and Coloumb friction law), for the same cyclic loading condition and material considered in this paper, the reader is refered to [15].

For fair comparison, all meshless results in this section are also computed on the nodes extracted from ABAQUS meshes (Figure 3).

In MLSM, $n = 25$ support nodes and $m = 15$ Gaussian basis functions, defined as follows, are used

$$b_i(\boldsymbol{x}) = \exp(\|\boldsymbol{x} - \boldsymbol{x}_i\|^2/\tau^2), \tag{26}$$

with $\tau = 150\delta r(\boldsymbol{x}_i)$, where $\delta r(x)$ is the distance to the closest neighbor of x_i. In MLS approximations, Gaussian weight with $\tau = \delta r(\boldsymbol{x}_i)$ was used. In MLPG computations, MLS approximation over 13 closest nodes was used, with MLS weight defined as

$$w(\boldsymbol{x}) = \omega(\|\boldsymbol{x}\|/r(\boldsymbol{x})), \quad \omega(\rho) = \begin{cases} 1 - 6\rho^2 + 8\rho^3 - 3\rho^4 & \rho \le 1, \\ 0 & \rho > 1, \end{cases} \tag{27}$$

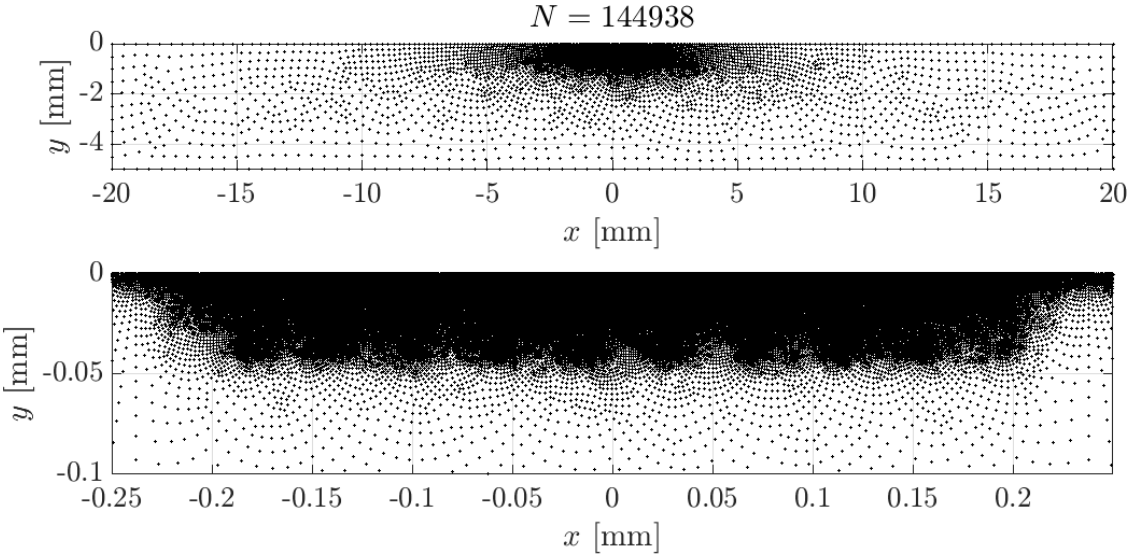

Figure 3: Nodes from the densest ABAQUS mesh used in $R = 10\,\text{mm}$, $\mu = 0.3$ case.

where $r(\boldsymbol{x})$ is the average distance from $\boldsymbol{x}$ to its 13th and 14th closest node. The integration domain size d_i was set to $d_i = 0.7r(\boldsymbol{x}_i)$, the 2D integrals were approximated with Gaussian quadrature with 9 points and line integrals were approximated using 3 points.

In Figure 4 the von Mises stress is presented for all the four cases defined in Table 1. The informative plots in Figure 4 are generated from results computed by MLSM.

As already noted in [15], the surface traction σ_{xx} is of particular interest due to its volatile behavior on the boundary of the stick and slip zones. The maximal surface traction is a good indicator of possible damage location, and can be used as a guide for crack initiation. It is therefore crucial that this value is computed as accurately as possible, which is a challenging task. For illustration, in case of $R = 10\,\text{mm}$, the contact area is approximately 100 times smaller than domain length L, and the stress on the edge of the contact is concentrated only on a small portion of the contact area. Extensive refinement is needed to even obtain the correct shape of the stress profile on the top, and even more so to determine it accurately. In Figure 5, stress $\sigma_{xx}(x, 0)$ under the contact, computed with MLSM, MLPG and ABAQUS, is presented. It can be seen that all three approaches capture the general behavior of the observed stress field, and that the results agree well.

Because of the significance of the maximal stress, a more precise analysis was done by comparing the maximal stress σ_{xx} on the top of the domain

$$\sigma_{xx}^{\max} := \max_{x \in [-2a, 2a]} \sigma_{xx}(x, 0), \tag{28}$$

with respect to the mesh size, measured in number of nodes under the contact (Figure 6). We present this study in Figure 6, where we observe a different behavior between the strong form method MLSM and the weak form methods MLPG and ABAQUS (FEM). For ABAQUS, we used two types of elements, namely, CPE4R and CPE8R, where the former represents a linear element and the latter represents a quadratic element. Both the weak form methods, MLPG and ABAQUS behave similarly, while the strong form method MLSM shows different pattern. Nevertheless, they all seem to converge in the asymptotic range (when the number of nodes is sufficiently high). Note that the results of MLPG lie nicely between the CPE4R results and the CPE8R results. More importantly, the results of MLPG are obtained on the same number of nodes that are used by CPE4R elements. This shows that for this problem, MLPG delivers higher accuracy than ABAQUS. The difference between MLPG and ABAQUS results can be attributed to the fact that in ABAQUS, the CPE4R elements are used (with reduced integration), whereas in MLPG, the 2D integrals are approximated

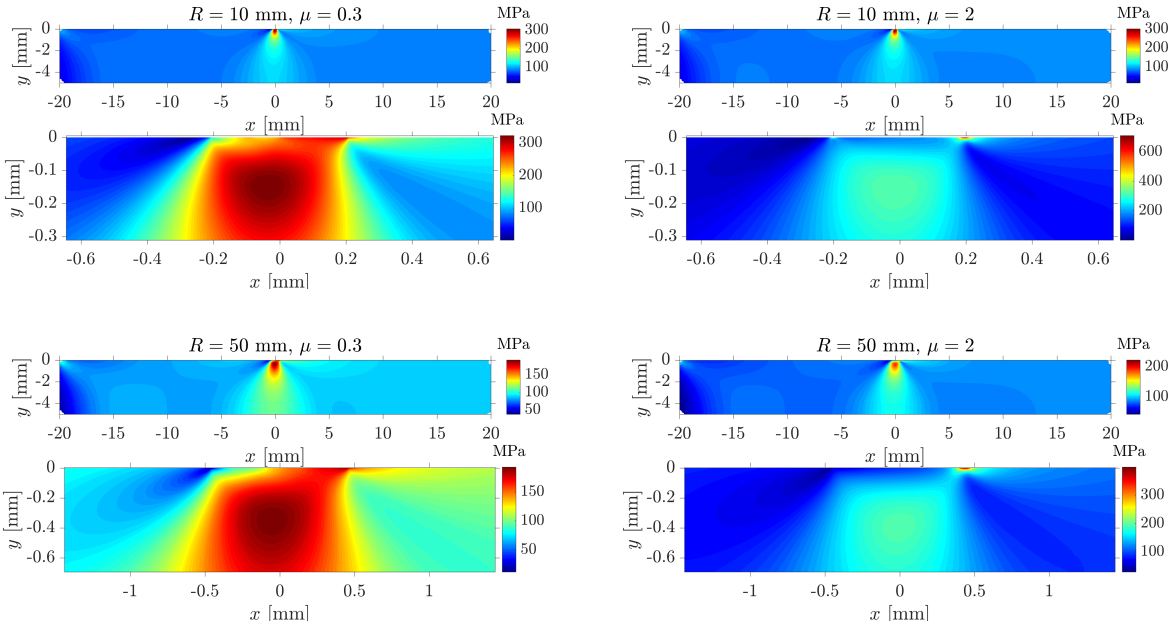

Figure 4: Von Mises stress of four considered cases computed by MLSM on densest meshes. In each panel, a stress in a whole specimen is shown on the top, followed by a magnified picture showing only the region under the contact area.

with Gaussian quadrature with 9 points, and line integrals with 3 points. These points in MLPG are sufficient for approximating an integral of the product of two quadratic functions.

To get a better insight into this phenomenon, two groups of plots are presented in Figure 7 for the case $R = 10$ mm and $\mu = 2$. In the upper two panels, σ_{xy} profiles are provided for all three methods (ABAQUS with two different type of elements), for different numbers of nodes under the contact. Note that σ_{xy} should reproduce boundary condition q, and therefore, we can compare the computed results against the prescribed condition, which is marked as "Exact". The same, even more pronounced effect, is present in the computation of σ_{xx} (bottom two panels) of Figure 7. All plots confirm that to capture the peak in the stress, the weak form methods require more nodes in comparison to the strong form method. This observation of weak form methods aligns with the typical observations from FEM studies, that more points are required to approximate sharp peaks and high gradient functions. However, in this particular case, the MLSM shows considerably more accurate results, even when ABAQUS uses twice the number of nodes (with CPE8R elements).

The reason behind this behavior is not clear, and could be attributed to the sensitivity of the strong form solution to point placement as well as the tendency of weak form based methods to smooth sharp gradients. This tendency can be overcome by, for example, e adaptivity in (enriched) finite element methods, and adaptive enrichment schemes for moving singularities and discontinuities.

The important factor of the numerical solution is its computational time. We executed all three solution procedures on server with 16-core Intel® Xeon® Gold 6130 Processors running CentOS 7.4 operating system. Execution times of both meshless methods are, as expected, longer in comparison to the ABAQUS solution, since we are comparing research code of a prototype algorithm to a fully optimized code of a mature method. Nevertheless, the computation times are comparable, e.g. ABAQUS with CPE4R elements needed 17 s to solve problem on $N = 45686$ nodes, while MLSM and MLPG required 25 s and 56 s, respectively.

4.2. Solution on meshless nodal distribution

Results presented in Section 4.1 have been computed on the nodes from the ABAQUS software that relies on meshing. A simple nodal positioning algorithm has been developed which does not require any

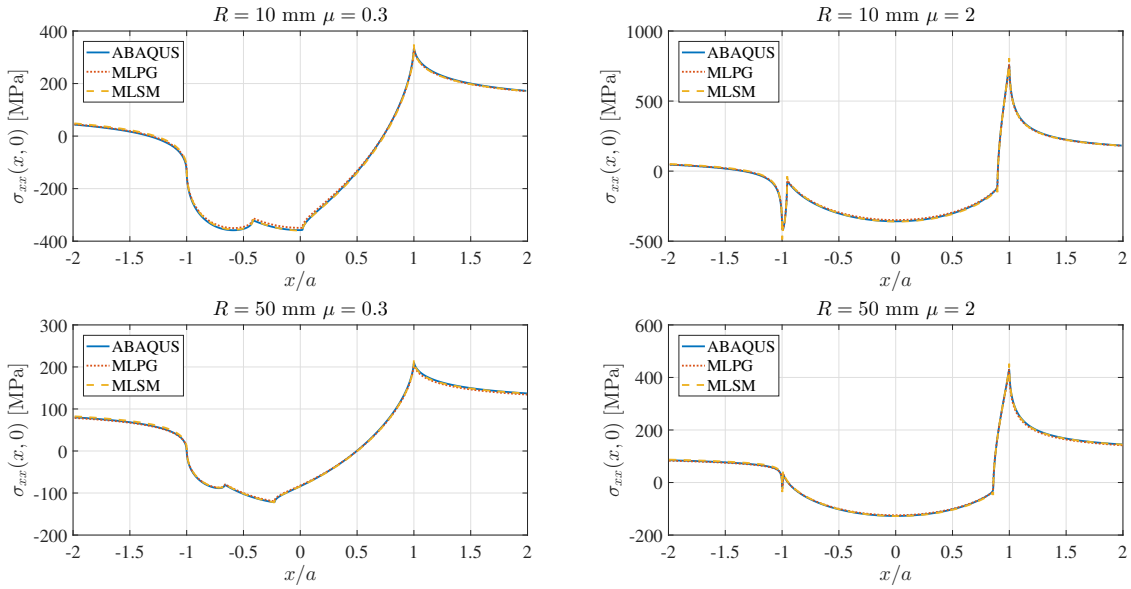

Figure 5: Surface stress $\sigma_{xx}(x, 0)$ under contact, computed with three different methods. ABAQUS results are CPE4R elements.

mesh generation. Although meshless methods do not need a structured mesh, and in some cases even randomly positioned nodes can be used [48], it is well-known that using regularly distributed nodes leads to more accurate and stable results [26, 49, 50].Therefore, despite the apparent robustness of meshless methods regarding nodal distributions, certain efforts are to be invested into node placement [51], with the ultimate goal to maximize stability and accuracy, and to retain the generality of the meshless principle. A possible approach to achieve this goal is to distribute nodes with a quite simple algorithm based on Poisson Disc Sampling. Such algorithms have been already used in a meshless context [52]. First, a seed node is positioned randomly within the domain. Then, new nodes are added on the circle centered at the seed node and with a radius supplied as a desired nodal density parameter (δr), i.e. the value $\delta r(x, y)$ represents the desired distance between node with coordinates (x, y) and its closest neighbor. In the next iteration, one of the newly added nodes is selected as the new seed node, and the procedure is repeated. The most expensive part of the algorithm is to check if newly positioned node violates proximity criterion, i.e. if a newly added node is positioned too close to any of already positioned nodes. The search can be efficiently implemented with k-d tree or some similar structure. To solve the problem at hand, we use the following δr function

$$\delta r(x, y) = d^{\alpha}(\Delta x - \delta x) + \delta x, \qquad d = \min\{d_1, d_2, d_3, d_4, 1\},$$

where

$$\begin{aligned} d_1 &= \left\| \left(\tfrac{x-(-a)}{\eta_x}, \tfrac{y}{\eta_y} \right) \right\|, & d_2 &= \left\| \left(\tfrac{x-a}{\eta_x}, \tfrac{y}{\eta_y} \right) \right\|, \\ d_2 &= \left\| \left(\tfrac{x-(e+c)}{\eta_x}, \tfrac{y}{\eta_y} \right) \right\|, & d_4 &= \left\| \left(\tfrac{x-(e-c)}{\eta_x}, \tfrac{y}{\eta_y} \right) \right\|, \end{aligned} \tag{29}$$

and η_x, η_y are scaling parameters with $\eta_x = \frac{3}{4}L$, $\eta_y = \frac{6}{10}W/2$. Values $\Delta x = \frac{1}{100}L$ and $\alpha = 1.2$ were used in all discretizations, while δx varied to produce nodal distributions with different densities. Meshes for exponentially spaced δx were generated for each case, with δx ranging from $0.025\Delta x$ to $0.00014\Delta x$, resulting in final discretization begin approximately 7200 times denser under the contact region than on the other boundaries. A sample mesh generated using the proposed distribution function (29) is shown in Figure 8.

Using the proposed nodal distribution instead of the ABAQUS mesh, the results for $\sigma_{xx}^{\max}$ from Figure 6 have been reproduced, and are shown in Figure 9 for both the meshless methods. As expected, we observe similar behavior as with ABAQUS meshes. The non-smooth convergence plots are an artifact of more

irregular node positions. Contrary to ABAQUS meshes, where one element (and consequently one node) is always put on the edge of the contact area, the nodes placed using the method described above pay no attention to contact zone boundaries. Therefore, when imposing boundary conditions, some variation in capturing high stress values is to be expected.

5. Conclusions

In this paper, we introduced meshless methods for stress computation in a typical fretting fatigue simulation. The results are first compared to the well-established ABAQUS software, and they are found to be in good agreement. The weak form MLPG behaves similarly to the ABAQUS solution, which is also based on a weak form method (FEM). However, in this particular case, the strong form meshless method (MLSM) shows different behavior. It performs notably better in capturing the peak surface stress, which is a crucial solution value in the fretting fatigue simulation as it directly influences the crack initiation. This strong form meshless method provides an accurate maximal stress with a significantly lower number of nodes under the contact, which could be an advantage in fretting fatigue simulations with high number of cycles.

Our future research will be devoted to devising automatic error estimation and mesh adaptation approaches for generalized finite differences and point collocation schemes [53, 54, 55, 45]. We will also investigate optimal point placement and stencil selection [56, 40], as well as local enrichment for both, point collocation and Galerkin methods, to accelerate convergence.

Acknowledgments

The authors would like to acknowledge the financial support of the Research Foundation Flanders (FWO), The Luxembourg National Research Fund (FNR) and Slovenian Research Agency (ARRS) in the framework of the FWO Lead Agency project: G018916N Multi-analysis of fretting fatigue using physical and virtual experiments.

References

[1] H.-K. Jeung, J.-D. Kwon, C. Y. Lee, Crack initiation and propagation under fretting fatigue of inconel 600 alloy, J. Mech. Sci. Technol 29 (2015) 5241–5244. doi:10.1007/s12206-015-1124-8.

[2] D. A. Hills, D. Nowell, Mechanics of Fretting Fatique, Springer Science+Business Media, Dordrecht, 1994. doi:10.1007/978-94-015-8281-0.

[3] O. J. McCarthy, J. P. McGarry, S. B. Leen, The effect of grain orientation on fretting fatigue plasticity and life prediction, Tribol. Int. 76 (2014) 100–115. doi:10.1016/j.triboint.2013.09.023.

[4] A. de Pannemaecker, J. Y. Buffiere, S. Fouvry, O. Graton, In situ fretting fatigue crack propagation analysis using synchrotron X-ray radiography, Int. J. Fatigue 97 (2017) 56–69. doi:10.1016/j.ijfatigue.2016.12.024.

[5] E. Giner, M. Sabsabi, J. J. Ródenas, F. J. Fuenmayor, Direction of crack propagation in a complete contact fretting-fatigue problem, Int. J. Fatigue 58 (2014) 172–180. doi:10.1016/j.ijfatigue.2013.03.001.

[6] N. Noraphaiphipaksa, A. Manonukul, C. Kanchanomai, Fretting fatigue with cylindrical-on-flat contact: Crack nucleation, crack path and fatigue life, Materials 10 (2) (2017) 155. doi:10.3390/ma10020155.

[7] R. Hojjati-Talemi, M. A. Wahab, J. De Pauw, P. De Baets, Prediction of fretting fatigue crack initiation and propagation lifetime for cylindrical contact configuration, Tribol. Int. 76 (2014) 73–91. doi:10.1016/j.triboint.2014.02.017.

[8] M. J. Sabsabi, E. Giner, F. J. Fuenmayor, Experimental fatigue testing of a fretting complete contact and numerical life correlation using X-FEM, Int. J. Fatigue 33 (6) (2011) 811–822. doi:10.1016/j.ijfatigue.2010.12.012.

[9] K. J. Kubiak, T. G. Mathia, Influence of roughness on contact interface in fretting under dry and boundary lubricated sliding regimes, Wear 267 (1-4) (2009) 315–321. doi:10.1016/j.wear.2009.02.011.

[10] S. Fouvry, P. Kapsa, L. Vincent, K. D. Van, Theoretical analysis of fatigue cracking under dry friction for fretting loading conditions, Wear 195 (1-2) (1996) 21–34. doi:10.1016/0043-1648(95)06741-8.

[11] P. J. Golden, T. Nicholas, The effect of angle on dovetail fretting experiments in Ti-6Al-4V, Fatigue & fracture of engineering materials & structures 28 (12) (2005) 1169–1175. doi:10.1111/j.1460-2695.2005.00956.x.

[12] T. Yue, M. A. Wahab, Finite element analysis of stress singularity in partial slip and gross sliding regimes in fretting wear, Wear 321 (2014) 53–63. doi:10.1016/j.wear.2014.09.008.

[13] T. Zhang, P. E. McHugh, S. B. Leen, Computational study on the effect of contact geometry on fretting behaviour, Wear 271 (9-10) (2011) 1462–1480. doi:10.1016/j.wear.2010.11.017.

[14] I. Svetlizky, J. Fineberg, Classical shear cracks drive the onset of dry frictional motion, Nature 509 (2014) 205–208. doi:10.1038/nature13202.

[15] K. Pereira, S. Bordas, S. Tomar, R. Trobec, M. Depolli, G. Kosec, M. Abdel Wahab, On the convergence of stresses in fretting fatigue, Materials 9 (8) (2016) 639. doi:10.3390/ma9080639.

[16] R. Kruse, N. Nguyen-Thanh, L. De Lorenzis, T. J. R. Hughes, Isogeometric collocation for large deformation elasticity and frictional contact problems, Comput. Methods Appl. Mech. Eng. 296 (2015) 73–112. doi:10.1016/j.cma.2015.07.022.

[17] P. Huang, X. Zhang, S. Ma, X. Huang, Contact algorithms for the material point method in impact and penetration simulation, Int. J. Numer. Methods Eng. 85 (4) (2011) 498–517.

[18] S. Li, D. Qian, W. K. Liu, T. Belytschko, A meshfree contact-detection algorithm, Comput. Methods Appl. Mech. Eng. 190 (24-25) (2001) 3271–3292. doi:10.1016/s0045-7825(00)00392-3.

[19] O. C. Zienkiewicz, R. L. Taylor, The Finite Element Method: Solid Mechanics, Butterworth-Heinemann, 2000.

[20] V. P. Nguyen, T. Rabczuk, S. Bordas, M. Duflot, Meshless methods: A review and computer implementation aspects, Math. Comput. Simul 79 (3) (2008) 763–813. doi:10.1016/j.matcom.2008.01.003.

[21] B. Mavrič, B. Šarler, Local radial basis function collocation method for linear thermoelasticity in two dimensions, Int. J. Numer. Methods Heat Fluid Flow 25 (2015) 1488–1510. doi:10.1108/hff-11-2014-0359.

[22] J. Slak, G. Kosec, Refined Meshless Local Strong Form solution of Cauchy–Navier equation on an irregular domain, Eng. Anal. Boundary Elem.doi:10.1016/j.enganabound.2018.01.001.

[23] J. Slak, G. Kosec, Adaptive radial basis function–generated finite differences method for contact problems, Int. J. Numer. Methods Eng.doi:10.1002/nme.6067.

[24] L. Sang-Ho, Y. Young-Cheol, Meshfree point collocation method for elasticity and crack problems, Int. J. Numer. Methods Eng. 61 (2004) 22–48. doi:10.1002/nme.1053.

[25] G. R. Liu, Y. T. Gu, An Introduction to Meshfree Methods and Their Programming, Springer, Dordrecht, 2005.

[26] R. Trobec, G. Kosec, Parallel scientific computing: theory, algorithms, and applications of mesh based and meshless methods, Springer, 2015.

[27] T. J. R. Hughes, J. A. Cottrell, Y. Bazilevs, Isogeometric analysis: CAD, finite elements, NURBS, exact geometry and mesh refinement, Comput. Methods Appl. Mech. Engrg. 194 (2005) 4135–4195. doi:10.1016/j.cma.2004.10.008.

[28] P. S. Jensen, Finite difference technique for variable grids, Comput. Struct. 2 (1972) 17–29. doi:10.1016/0045-7949(72)90020-x.

[29] T. Liska, J. Orkisz, The finite difference method at arbitrary irregular grids and its application in applied mechanics, Comput. Struct. 2 (1980) 83–95. doi:10.1016/0045-7949(80)90149-2.

[30] J. Orkisz, Meshless finite difference method I. Basic approach, II. Adaptive approach, in: D. Idelshon, Oñate (Ed.), Computational mechanics, IACM, CINME, 1998.

[31] B. Šarler, A radial basis function collocation approach in computational fluid dynamics, CMES: Computer Modeling in Engineering and Sciences 7 (2005) 185–193.

[32] C. Prax, H. Sadat, E. Dabboura, Evaluation of high order versions of the diffuse approximate meshless method, Appl. Math. Comput. 186 (2007) 1040–1053. doi:10.1016/j.amc.2006.08.059.

[33] J.-S. Chen, M. Hillman, S.-W. Chi, Meshfree methods: progress made after 20 years, J. Eng. Mech. 143 (4) (2017) 04017001. doi:10.1061/(asce)em.1943-7889.0001176.

[34] T. Rabczuk, P. M. A. Areias, T. Belytschko, A meshfree thin shell method for non-linear dynamic fracture, Int. J. Numer. Methods Eng. 72 (5) (2007) 524–548. doi:10.1002/nme.2013.

[35] S. Bordas, T. Rabczuk, G. Zi, Three-dimensional crack initiation, propagation, branching and junction in non-linear materials by an extended meshfree method without asymptotic enrichment, Eng. Fract. Mech. 75 (5) (2008) 943–960. doi:10.1016/j.engfracmech.2007.05.010.

[36] J. J. Monaghan, Smoothed particle hydrodynamics, Annu. Rev. Astron. Astrophys. 30 (1992) 543–574. doi:10.1146/annurev.aa.30.090192.002551.

[37] T. Belytschko, Y. Y. Lu, L. Gu, Element-free Galerkin methods, Int. J. Numer. Methods Engrg. 37(2) (1994) 229–256. doi:10.1002/nme.1620370205.

[38] F. Auricchio, L. B. D. Veiga, T. J. R. Hughes, A. Reali, G. Sangalli, Isogeometric collocation methods, Math. Models Methods Appl. Sci. 20 (2010) 2075. doi:10.1142/S0218202510004878.

[39] H. Wendland, Scattered Data Approximation, Cambridge University Press, 2004. doi:10.1017/cbo9780511617539.

[40] O. Davydov, R. Schaback, Optimal stencils in Sobolev spaces, IMA J. Numer. Anal.doi:10.1093/imanum/drx076.

[41] S. N. Atluri, The Meshless Method (MLPG) for Domain and BIE Discretization, Tech Science Press, Forsyth, 2004.

[42] S. N. Atluri, T. Zhu, A new meshless local Petrov-Galerkin (MLPG) approach in computational mechanics, Comput. Mech. 22 (2) (1998) 117–127. doi:10.1007/s004660050346.

[43] D. Shepard, A two-dimensional interpolation function for irregularly-spaced data, in: Proceedings of the 1968 23rd ACM national conference, ACM, 1968, pp. 517–524. doi:10.1145/800186.810616.

[44] E. Onate, S. Idelsohn, O. C. Zienkiewicz, R. L. Taylor, A finite point method in computational mechanics: Applications to convective transport and fluid flow, Int. J. Numer. Methods Eng. 39 (22) (1996) 3839–3866. doi:10.1002/(sici)1097-0207(19961130)39:22¡3839::aid-nme27¿3.0.co;2-r.

[45] D. T. Oanh, O. Davydov, H. X. Phu, Adaptive RBF-FD method for elliptic problems with point singularities, Appl. Math. Comput. 313 (2017) 474–497. doi:10.1016/j.amc.2017.06.006.

[46] G. E. Fasshauer, J. G. Zhang, On choosing "optimal" shape parameters for RBF approximation, Numerical Algorithms 45 (1-4) (2007) 345–368. doi:10.1007/s11075-007-9072-8.

[47] R. Trobec, G. Kosec, M. Šterk, B. Šarler, Comparison of local weak and strong form meshless methods for 2-D diffusion equation, Eng. Anal. Boundary Elem. 36 (3) (2012) 310–321. doi:10.1016/j.enganabound.2011.08.009.

[48] K. Reuther, B. Šarler, M. Rettenmayr, Solving diffusion problems on an unstructured, amorphous grid by a meshless method, Int. J. Therm. Sci. 51 (2012) 16–22. doi:10.1016/j.ijthermalsci.2011.08.017.

[49] P. Suchde, J. Kuhnert, S. Schröder, A. Klar, A flux conserving meshfree method for conservation laws, Int. J. Numer. Methods Engrg. 112(3) (2017) 238–256. doi:10.1002/nme.5511.

[50] P. Suchde, J. Kuhnert, S. Tiwari, On meshfree GFDM solvers for the incompressible Navier–Stokes equations, Computers & Fluids 165 (2018) 1–12. doi:10.1016/j.compfluid.2018.01.008.

[51] G. Kosec, A local numerical solution of a fluid-flow problem on an irregular domain, Adv. Eng. Software 120 (2016) 36–44. doi:10.1016/j.advengsoft.2016.05.010.

[52] B. Fornberg, N. Flyer, Fast generation of 2-D node distributions for mesh-free PDE discretizations, Computers & Mathematics with Applications 69 (7) (2015) 531–544. doi:10.1016/j.camwa.2015.01.009.

[53] J. J. Benito, F. Urena, L. Gavete, R. Alvarez, An h-adaptive method in the generalized finite differences, Comput. Methods Appl. Mech. Engrg. 192(5) (2003) 735–759. doi:10.1016/S0045-7825(02)00594-7.

[54] F. Perazzo, R. Löhner, L. Perez-Pozo, Adaptive methodology for meshless finite point method, Adv. Eng. Softw. 39(3) (2008) 156–166. doi:10.1016/j.advengsoft.2007.02.007.

[55] O. Davydov, D. T. Oanh, Adaptive meshless centers and RBF stencils for Poisson equation, J. Comput. Phys. 230(2) (2011) 287–304. doi:10.1016/j.jcp.2010.09.005.

[56] O. Davydov, D. T. Oanh, On the optimal shape parameter for Gaussian radial basis function finite difference approximation of the Poisson equation, Comput. Math. Appl. 62(5) (2011) 2143–2161. doi:10.1016/j.camwa.2011.06.037.

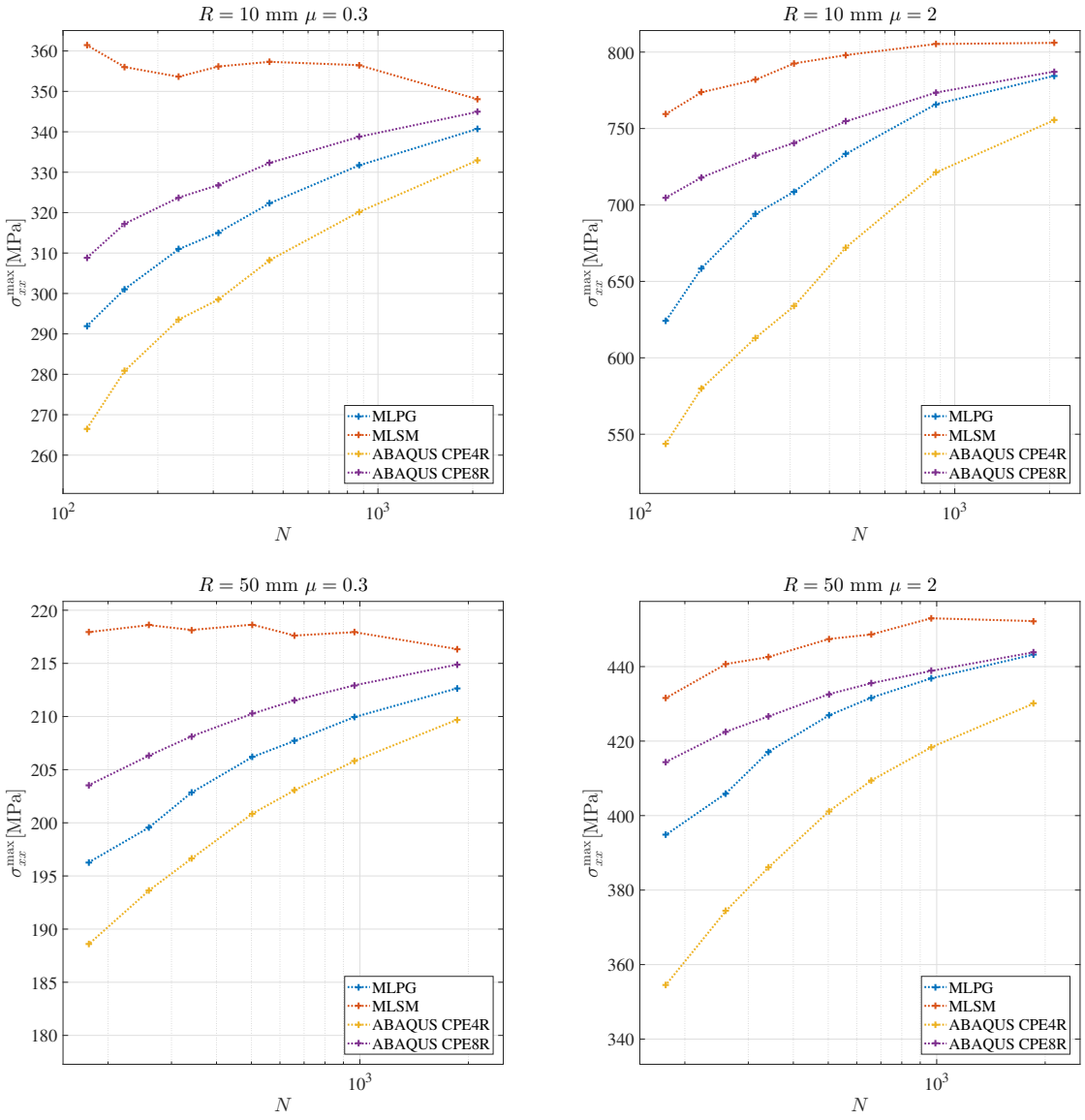

Figure 6: Maximal surface σ_{xx} under contact with respect to the number of nodes under the contact. Computed with MLPG, MLSM and ABAQUS (two element types, namely, CPE4R and CPE8R). MLPG and MLSM results are on the same number of nodes that are used by ABAQUS CPE4R elements.

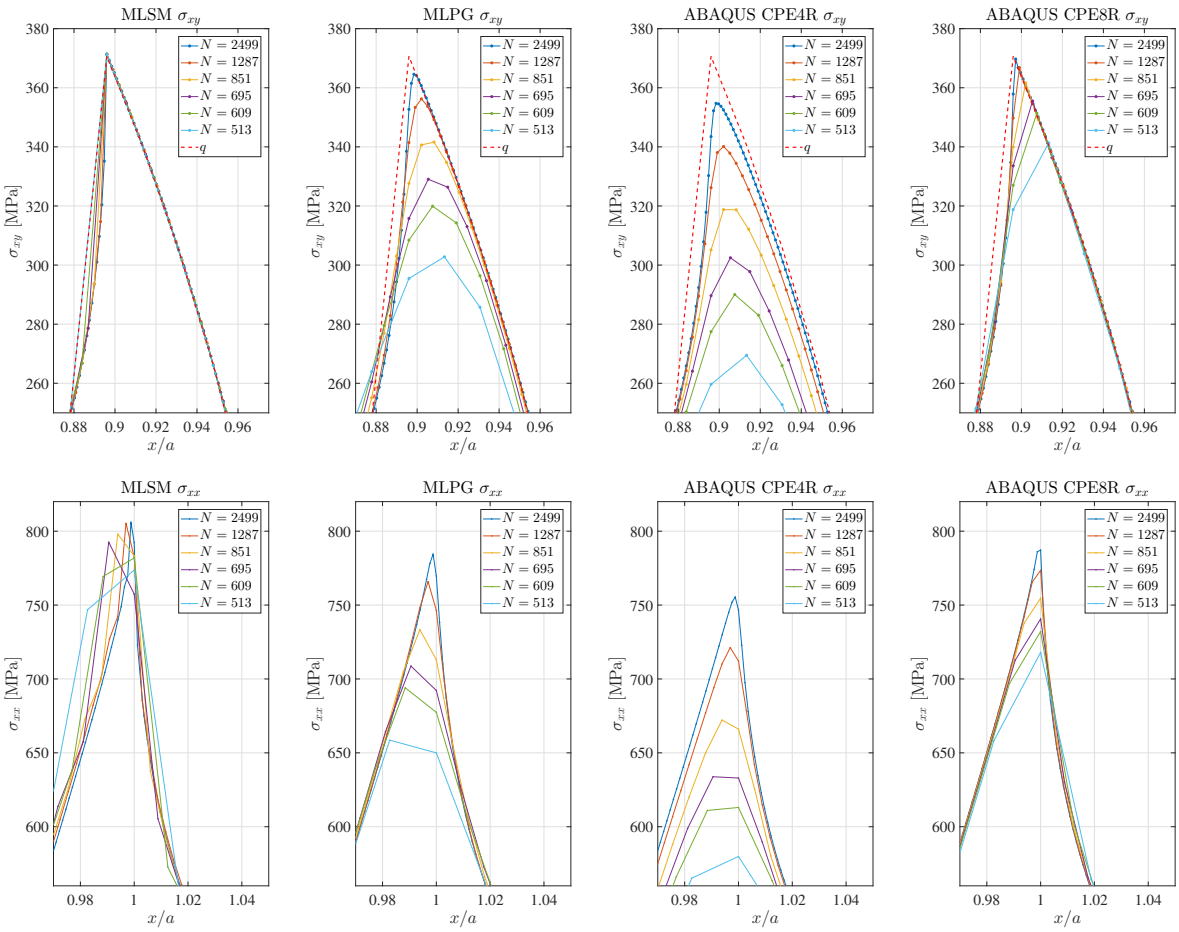

Figure 7: For case $R = 10\,\text{mm}$ and $\mu = 2$, the σ_{xy} (above) and σ_{xx} (below) surface stress profiles near the contact border.

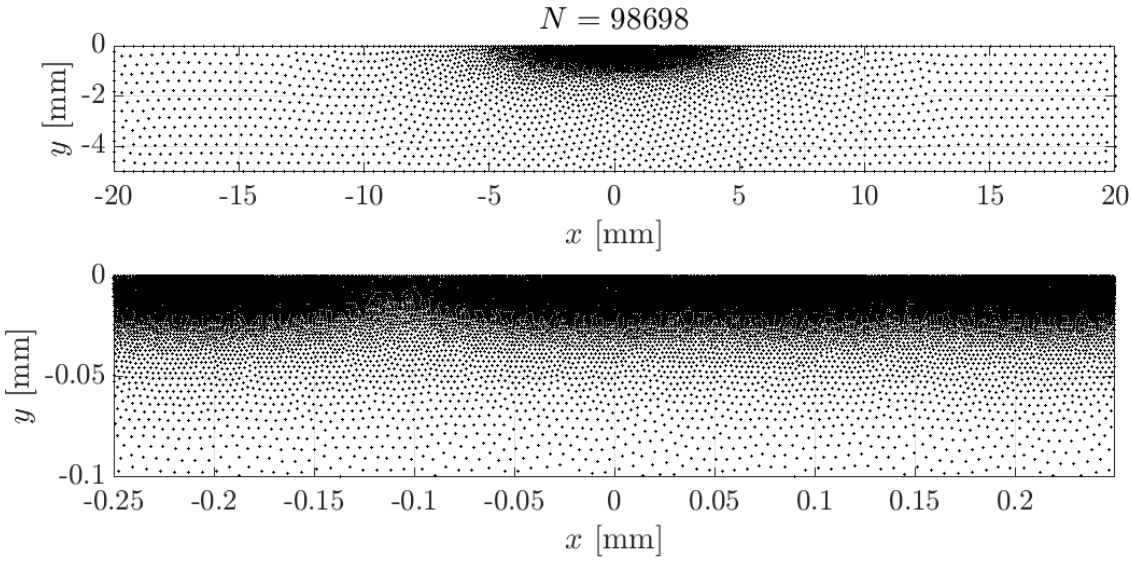

Figure 8: Nodes from the densest distribution with $\delta x = 2.7a \cdot 10^{-4}$ used in $R = 10\,\text{mm}$, $\mu = 0.3$ case.

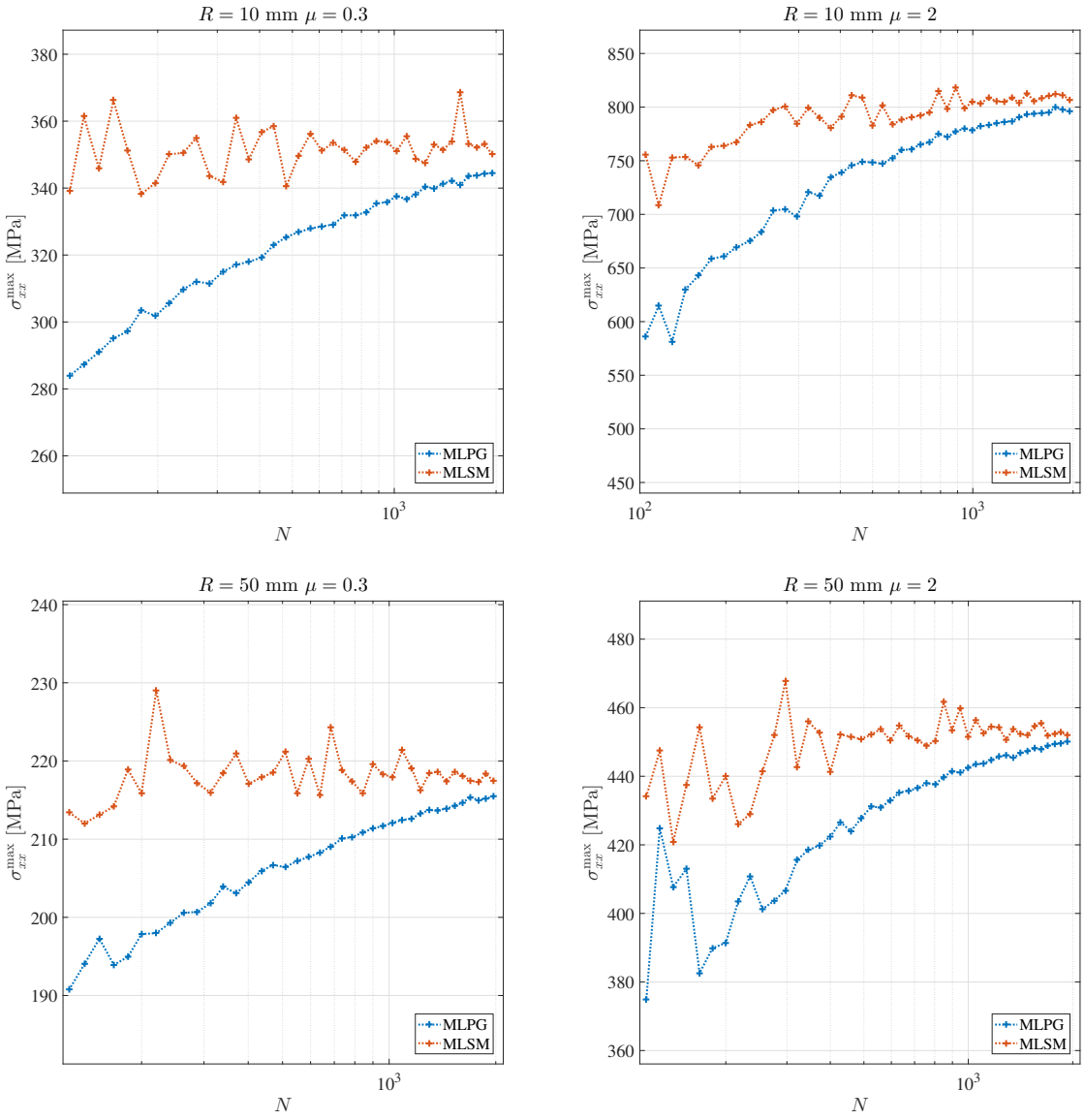

Figure 9: Maximal surface σ_{xx} under contact with respect to the number of nodes under the contact computed with MLPG and MLSM meshless methods on meshless nodal distributions.